Seismic Moment Tensors and Finite-Source Analysis of Chi-Chi Aftershocks

Douglas S. Dreger, Wu Cheng Chi, and Junkee Rhie
University of California
Berkeley Seismological Laboratory

Pacific Earthquake Engineering Research Center
University of California, Berkeley
January 2004

Abstract

Strong motion data for aftershocks of the September 1999 Chi-Chi, Taiwan earthquake sequence, compiled by PEER Lifelines, were investigated to determine seismic moment tensors, finite-source models, and to evaluate event locations. This data set provided by the Taiwan Central Weather Bureau consisted of strong motion accelerograms from 30 aftershocks with local magnitudes (M_L) between 4 to 6.8. Finite-source parameters were obtained for 6 of the large (M6+) aftershocks, seismic moment tensors for 4 of the M5+ aftershocks, and style of fault information for 15 of the aftershocks was determined. Analysis of event locations using both P and S-wave picks and a grid search routine indicates that the locations provided with the waveform data set are adequate for use in determining attenuation relationships.

Acknowledgements

Figures were prepared using Generic Mapping Tools (GMT) [Wessel and Smith, 1991].

"*This work was supported in part by the Pacific Earthquake Engineering Research Center through the Earthquake Engineering Research Centers Program of the National Science Foundation under Award number EEC-9701568*."

Table of Contents

List of Figures

List of Tables

1. Introduction

Waveform data for 30 aftershocks of the Mw7.6 September 1999 Chi-Chi Taiwan earthquake was investigated to evaluate event locations, compute seismic moment tensors, and where possible compute finite-source parameters for the largest events. In this data set there were 5 events with magnitude greater than 6. An additional magnitude 6 event on October 22, 1999 was added, and the strong motion data for this event was provided to Brian Chiou for attenuation analysis. There were 14 aftershocks with magnitudes greater that 5 in the provided data set. Table 1 lists the event information, and Figure 1 shows the locations of the events and the strong motion recording sites.

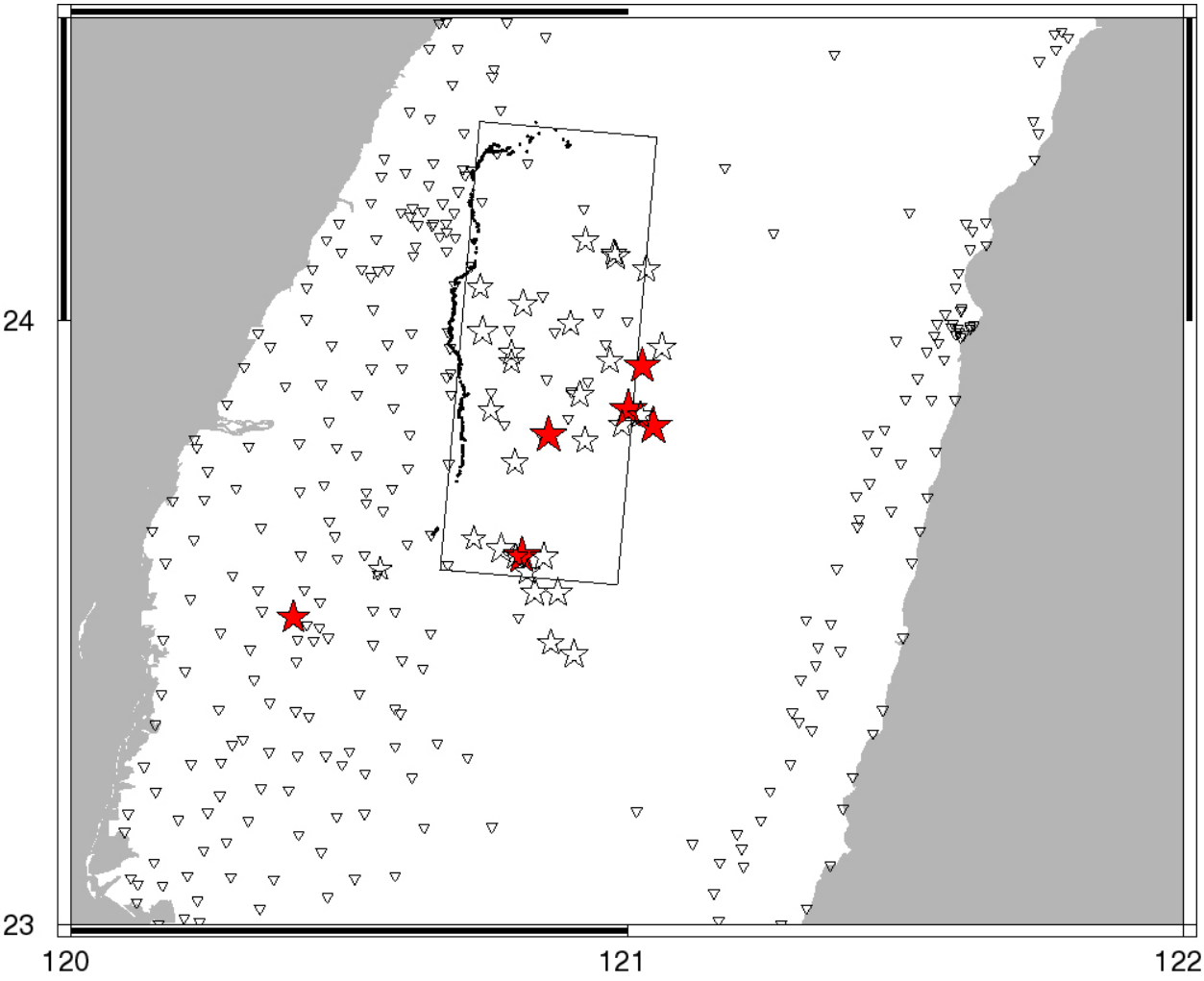

Figure 1.1 Location map showing strong motion stations (triangles), study events (stars), the surface trace of the mainshock (bold line), and the extent of the mainshock fault-plane model from Chi et al., 2001. The red stars highlight those events for which it was possible to obtain finite source parameters.

Table 1.1: Study Events

Date	Origin Time	N. Latitude	E. Longitude	Depth (km)	Magnitude
1999/09/20	18:03:41.16	23.8123	120.8590	8.19	6.60
1999/09/20	17:57:15.31	23.9255	121.0275	11.04	6.44
1999/09/20	18:21:28.60	23.9564	121.0630	9.68	5.22
1999/09/20	18:32:55.07	23.8290	120.9912	16.83	5.07
1999/09/20	18:34:25.90	23.8447	121.0239	21.28	4.90
1999/09/20	18:50:49.26	23.9346	120.9688	13.67	4.82
1999/09/20	18:56:04.45	23.7661	120.7985	9.22	4.72
1999/09/20	19:17:10.70	23.9329	120.7927	10.56	4.44
1999/09/20	19:19:49.62	23.9955	120.8981	19.46	4.64
1999/09/20	19:34:51.02	23.8531	120.7551	9.50	4.66
1999/09/20	19:40:32.57	23.5509	120.8759	7.40	5.28
1999/09/20	19:44:56.30	24.0561	120.7364	9.27	4.58
1999/09/20	19:57:52.63	24.0278	120.8134	11.98	5.19
1999/09/20	20:02:15.90	23.9823	120.7406	12.08	5.35
1999/09/20	20:08:11.41	24.1327	120.9252	10.96	4.75
1999/09/20	20:11:39.48	23.9480	120.7929	10.07	4.51
1999/09/20	20:21:59.67	24.1077	120.9795	11.12	5.22
1999/09/20	20:29:20.88	23.8024	120.9244	14.55	4.81
1999/09/20	21:23:23.86	23.6103	120.8510	10.07	4.92
1999/09/20	21:27:56.71	24.0851	121.0346	11.90	4.99
1999/09/20	21:39:53.71	23.5902	120.5561	14.13	4.11
1999/09/20	21:46:37.49	23.6121	120.8110	1.05	6.59
1999/09/20	21:54:47.08	23.6230	120.7741	4.31	5.33
1999/09/20	21:57:12.35	23.4682	120.8630	8.58	4.71
1999/09/20	22:15:33.96	23.5851	120.8208	2.77	4.66
1999/09/20	22:22:46.00	23.5510	120.8342	5.02	5.15
1999/09/20	22:33:54.81	24.1118	120.9770	12.79	4.75
1999/09/20	22:44:33.89	23.6402	120.7247	16.13	4.44
1999/09/20	22:56:45.85	23.8777	120.9151	11.62	4.93
1999/09/20	22:58:52.51	23.6111	120.7996	10.99	4.56
1999/09/20	23:18:13.21	23.4490	120.9052	9.57	5.10
1999/09/22	00:14:40.77	23.8260	121.0470	15.59	6.80
1999/09/25	23:52:49.63	23.8540	121.0020	12.06	6.80

The method that we used to determine seismic moment tensors utilizes data in the 0.02 to 0.05 Hz passband to reduce the impact of Earth structure on the inversion results, and has been found to yield robust results (e.g. Pasyanos et al., 1996; Fukuyama and Dreger, 2000). If noise levels are high in this passband then it becomes impossible to determine the seismic moment tensor. Unfortunately for a number of the events the noise in this passband is high. Since all events are on the same day the source of this noise is likely not microseismic, but rather long period coda from earlier large aftershocks. This reduced the number of events that it was possible to obtain moment tensors for to only four. In an effort to obtain additional focal parameter information we also studied the first motion picks. In cases where only first motions are available a mechanism is obtained but it was not possible to obtain the scalar moment and moment magnitude (M_W). It

was possible, however, to report on the style of faulting for all 15 of the $M_L \geq 5.0$ events. Finally, we developed a relationship between the reported M_L and M_W described in section 5.

Events with a magnitude of 6-6.5 have dimensions on the order of about 10 km that is large enough to produce a directivity signal that is discernable in data at local and regional distance. For these events we utilized the method of Dreger and Kaverina (2000) to determine the causative fault plane, scalar seismic moment, and the distribution of fault slip. In addition, we examined the sensitivity to hypocenter position, as well as the orientation of the fault plane, rise time and rupture velocity. For each event approximately 1000 inversions were performed to explore the parameter space of these variables (e.g. Chi and Dreger.; 2002; Chi and Dreger, 2004).

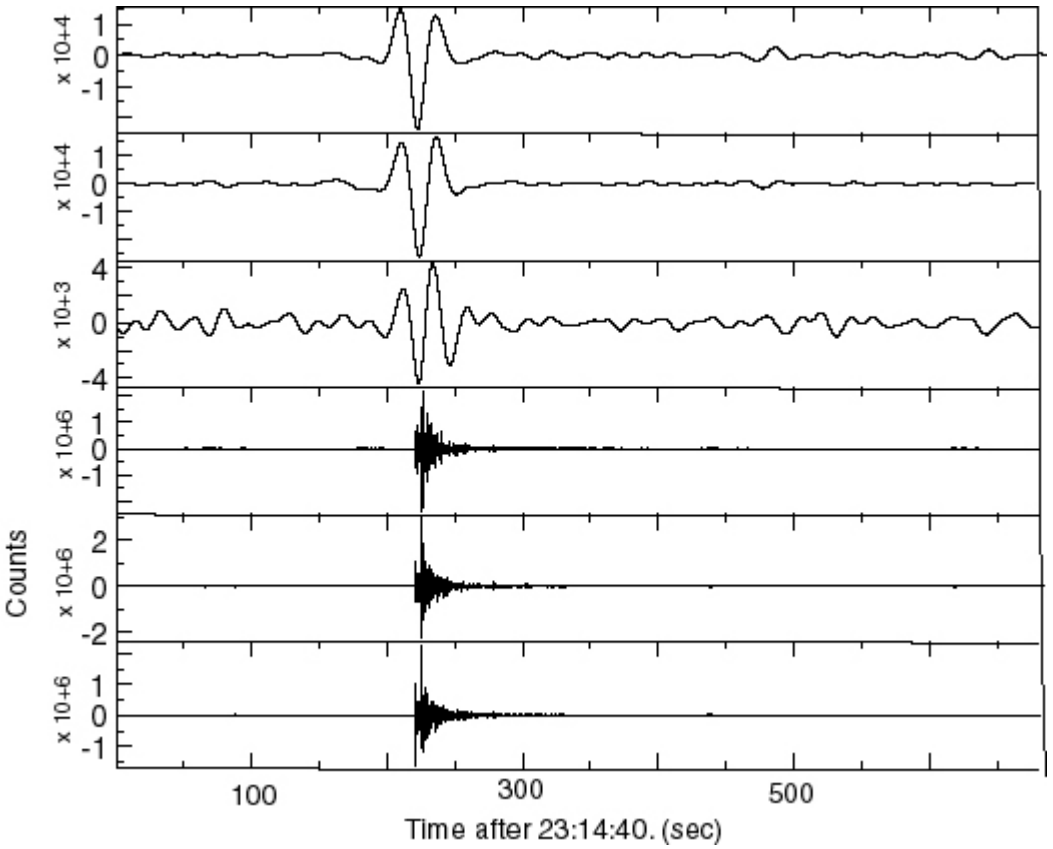

Figure 1.2 Comparison of raw velocity (lower three) and bandpass filtered (0.02 to 0.05 Hz) displacement seismograms recorded at Academia Sinica BATS station TPUB for the event at 23:18:13.2 (UTC). A seismic moment tensor was obtained for this event.

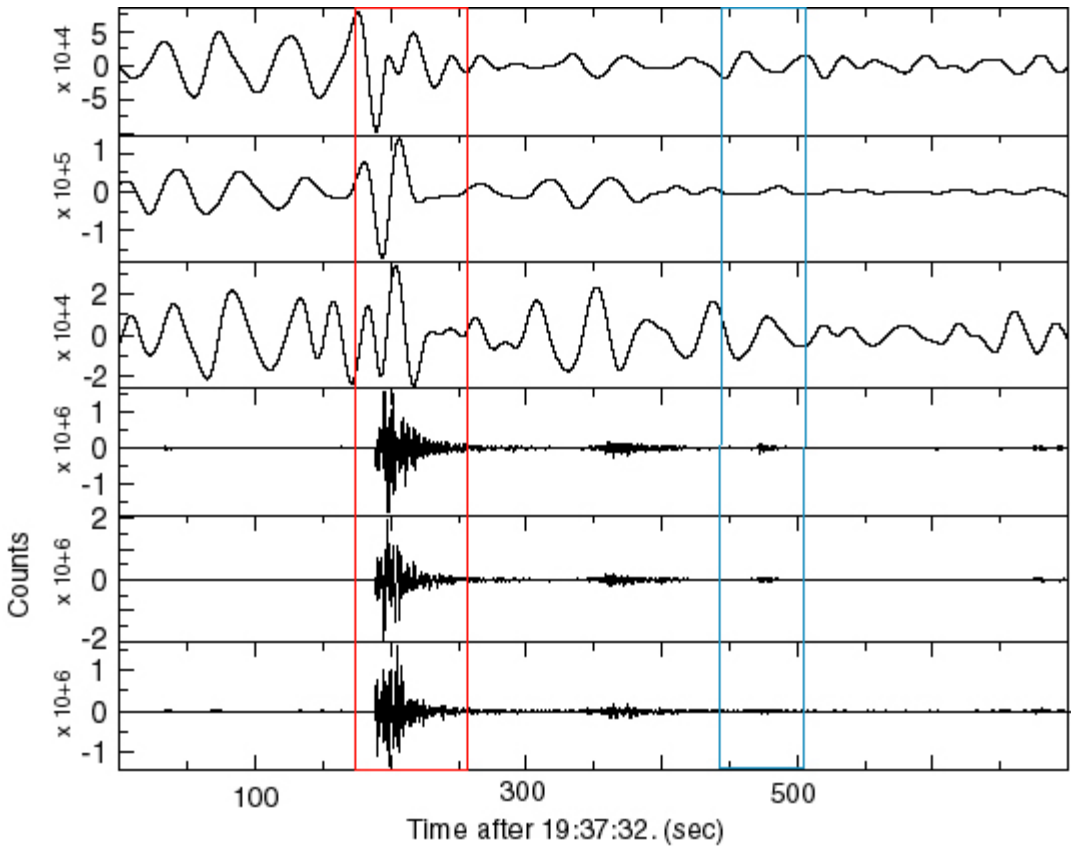

Figure 1.3 Comparison of raw velocity seismograms (lower three) and bandpass filtered (0.02 to 0.05 Hz) displacement (upper three) at Academia Sinica BATS station TPUB. The red lines bracket the M5.3 event at 19:40:32 UTC, and the blue lines bracket the M4.6 event at 19:44:56. For the 19:40 event a seismic moment tensor was obtained, however for the 19:44 event it was not possible to obtain a seismic moment tensor.

2. Event Locations

The hypocenters were evaluated using a grid search program (e.g. Dreger et al., 1998; Uhrhammer et al., 2001). P and S phase measurements were both used. This method computes arrival times for a gradient over a halfspace velocity model and calculates the arrival time residuals at each station for sources located throughout a 4-dimensional volume. The velocity model that was used reflects the average crustal velocity gradient in the multi-layered velocity model used in the seismic moment tensor and finite-fault analyses (Figure 2.1). The grid search is adaptive in the sense that if solutions are near the edges the grid creeps to center the minimum, and then collapses to sample the minimum with higher resolution. We use an initial model space that is large allowing the data to constrain the best solution. With the output of this program it is possible to directly inspect the goodness of fit parameter space to assess solution uniqueness and uncertainty. Figure 2.2 gives two representative examples that show the obtained locations are unique with well defined minima.

Since finite-source parameters were determined for all M6 events (section 4) event locations for only M5 events were determined. In each case approximately 100 phase readings (combining both P and S) were used. As shown in Figure 2.2 the quality of the location depends upon the station coverage, although in each case the initially reported location (white star) lies either in or at the edge of the minimum in the

traveltime residual. Table 2.1 lists the relocated hypocenters for the 9 M5 events. On average the relocations are 3.8±2.5 km in the horizontal with an overall range from 1.2 to 7.5 km. In the vertical the change in depth is large in some cases. Our inspection of the parameter space indicates that the source depth is poorly resolved. However, considering that the station geometry, velocity model, and location method differ from those used in preparing the initial event list provided to the project the relocated hypocenters are in close agreement. It is in our opinion that the original event locations may be used to calculate station distances for determining strong ground motion attenuation relationships. If the relocated hypocenters are to be used it is then recommended that when possible the relocated latitude and longitude should be combined with the source depth determined from the long-period seismic moment tensor results (see section 3).

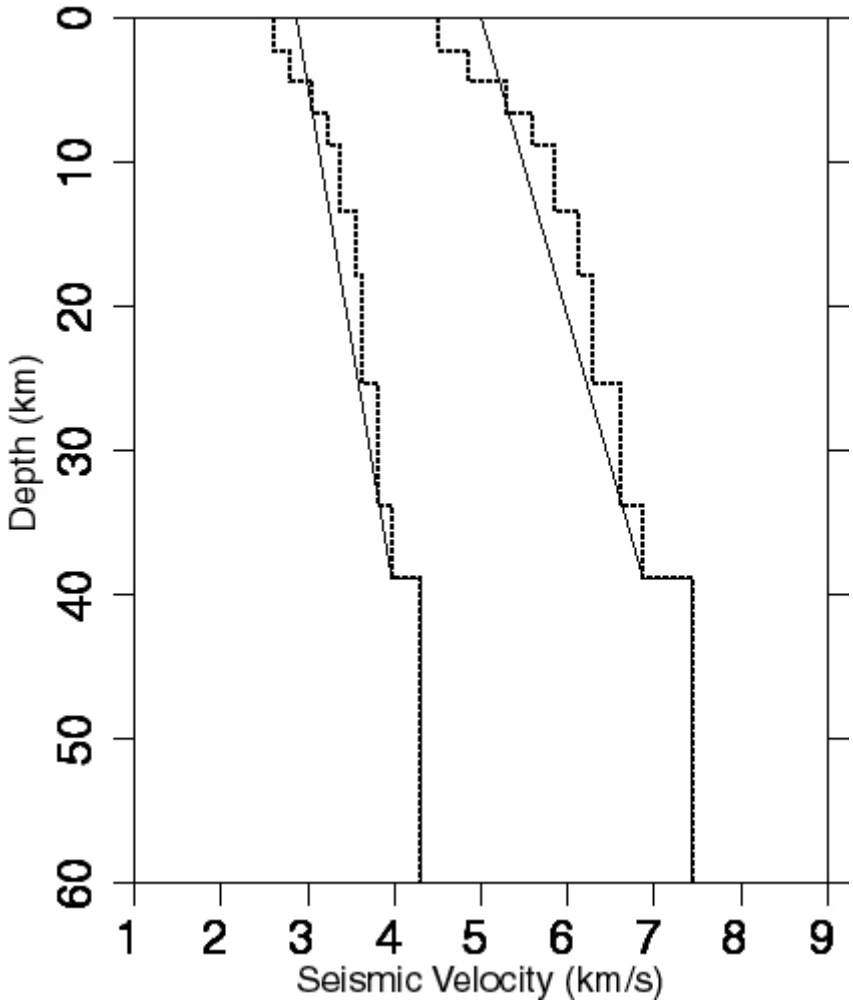

Figure 2.1 The gradient over a halfspace velocity model (solid) that was used to determine event locations is compared to the multi-layered velocity model (dashed) that was used to determine long-period seismic moment tensor solutions, and finite-source parameters (Chi et al., 2001). The gradient model was chosen to approximate the average gradient in the multi-layered velocity model.

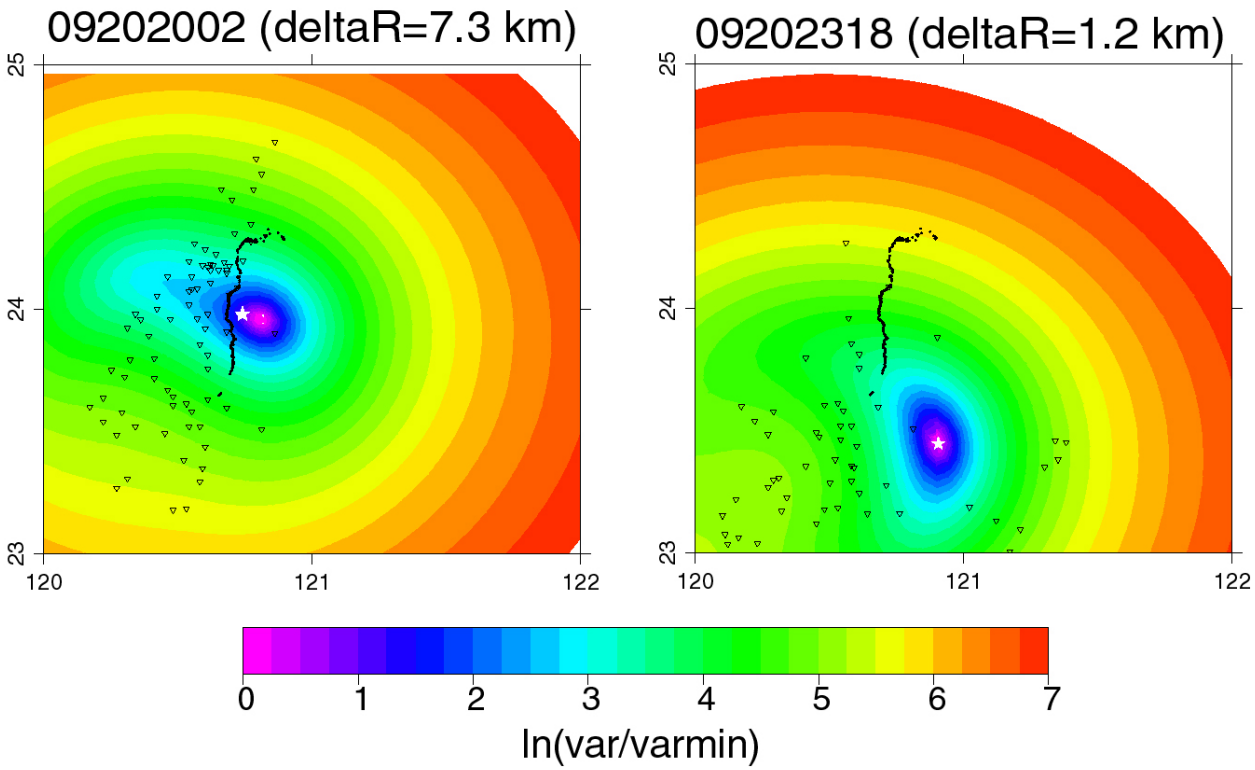

Figure 2.2 Examples of the location parameter space for two aftershocks. The mainshock fault trace is shown as the bold line, and the available strong motion stations for each event are shown as the inverted triangles. The color scaling shows the natural log of the ratio of the travel time variance at each point with respect to the lowest variance achieved. The central purple region gives the area of acceptable solutions, where the estimate travel time variance can be as large as factor of 1.28 larger than the minimum obtained in each case.

Table 2.1 Magnitude 5 event relocations

Date	Origin Time (UTC)	Mag.	Latitude	Longitude	Depth (reloc./original, km)	Mislocation (km)
1999/09/20	18:21:28.33	5.22	24.0014	121.0569	9.2/9.7	5.01
1999/09/20	18:32:54.34	5.07	23.8278	121.0026	20.5/16.8	1.17
1999/09/20	19:40:32.31	5.28	23.5614	120.8873	23.8/7.40	1.64
1999/09/20	19:57:51.32	5.19	24.0343	120.8872	12.0/23.6	7.53
1999/09/20	20:02:14.70	5.35	23.9588	120.8077	11.2/12.1	7.30
1999/09/20	20:21:59.33	5.22	24.1018	121.0052	11.2/11.1	2.69
1999/09/20	21:54:45.19	5.33	23.6229	120.8283	5.0/4.3	5.53
1999/09/20	22:22:45.67	5.15	23.5610	120.8569	11.7/5.0	2.57
1999/09/20	23:18:12.37	5.10	23.4597	120.9021	18.7/9.6	1.22

3. Seismic Moment Tensor Analysis

The complete, three-component waveform inversion method routinely employed by the BSL (e.g. Romanowicz et al., 1993; Pasyanos et al., 1996) was employed to compute the seismic moment tensors of events in Table 1.1. For events in the magnitude 5 and larger range we have found that an appropriate filter passband is 0.02 to 0.05 Hz. We inspected the strong motion

waveform data provided to the project by integrating to velocity and displacement and bandpass filtering using the corners stated above and found that generally the data was too noisy for the moment tensor analysis. Therefore we acquired broadband velocity data recorded by Academia Sinica's BATS array. This data proved to be more stable in the passband required for the moment tensor inversion, however as shown in Figures 1.2 and 1.3 for some of the events the noise level can be quite high. Since all of the events in Table 1.1 are on the same date the level of microseismic noise is considered to be the same for all of the events and the noise is likely due to the coda from larger aftershocks that are not on Table 1.1. Indeed there were 7 more M≥6 events during the study period (09/20/1999-09/25/1999). These events have not been studied and do present an opportunity to obtain additional finite-source information as described in section 4.

Green's functions were computed using a 1D models appropriate for the region (the layered model shown in Figure 2.1 from Chi et al., 2001) using a frequency/wave-number integration method.

As shown in Figure 3.1 well constrained moment tensor solutions are obtainable given sufficient signal-to-noise in the data. In this example for the event at 23:18 (UTC) we find that the solution yields a strike-slip mechanism. We performed inversions for all of the events over a range of source depth from 1 to 23 km, every 2 km. For event 23:18 (UTC) the resolution of the source depth is found to be not very good, where the goodness of fit parameter (variance reduction) is relatively flat over the whole range (Figure 3.2). The best depth obtained (13 km) is intermediate between the values originally reported and determined from the event relocation (section 2). It is noted that for some of the events studied the resolution of the focal depth was better. Figure 3.3 shows the result obtained by Honn Gao for this event which is very similar to the result we obtained. In cases where Honn Gao had solutions we find good correspondence between his and ours. Table 3.1 compiles the moment tensor results for events that we were able to obtain solutions for.

To obtain style of faulting information for more of the M≥5 aftershocks we investigated the first-motions. The first motions were picked from the acceleration records provided to the project. The first motions for events with moment tensors agree with the moment tensor solutions (Figure 3.4). Table 3.2 lists the focal parameters for the better constrained first motion data sets, and for all of the M≥5 the style of faulting was determined. The 5≤M≤6 data set contains reverse, oblique-reverse, and strike-slip events.

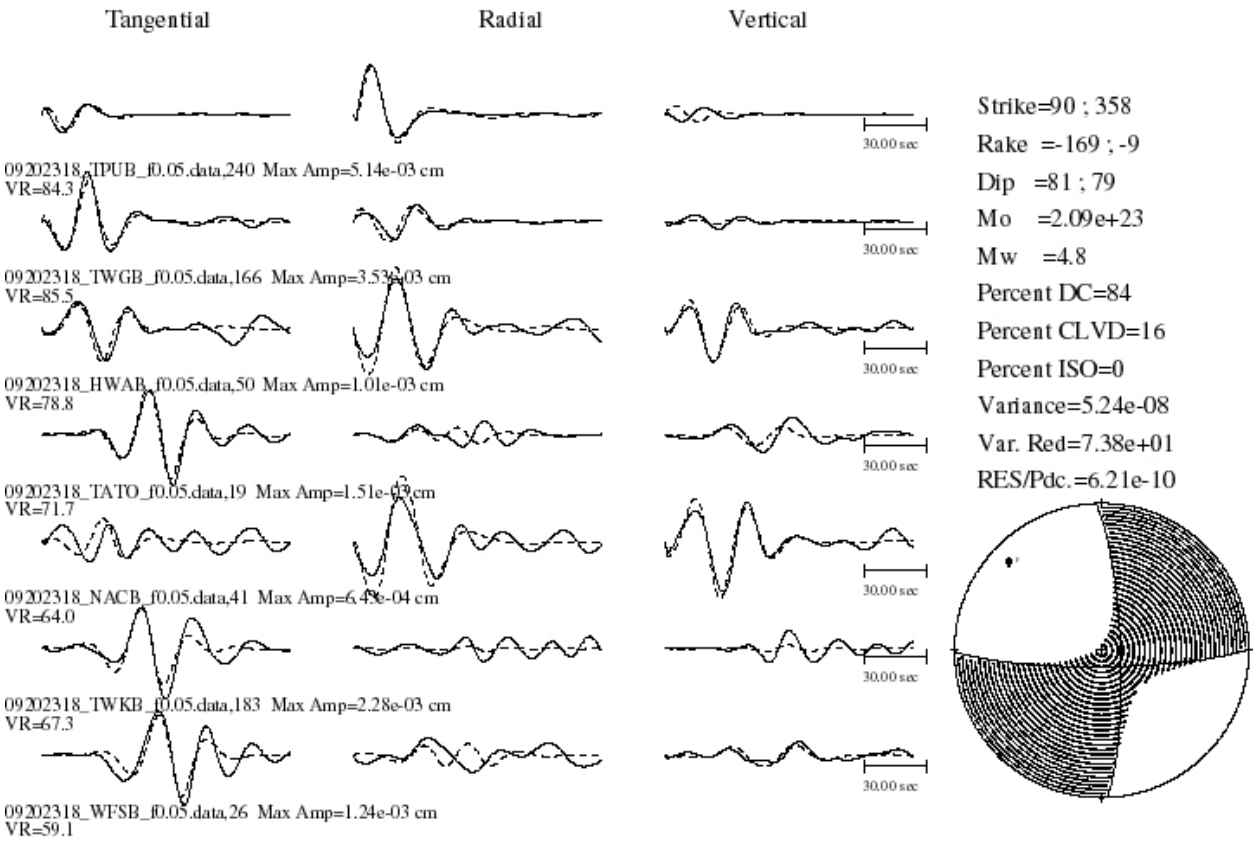

Figure 3.1. Example of seismic moment tensor inversion for the aftershock at 23:18 (UTC). This inversion utilized the broadband waveform data from the BATS array at 7 stations. The observed displacement waveforms are shown as solid lines, and the synthetics are dashed. This solution is for a best depth of 13 km.

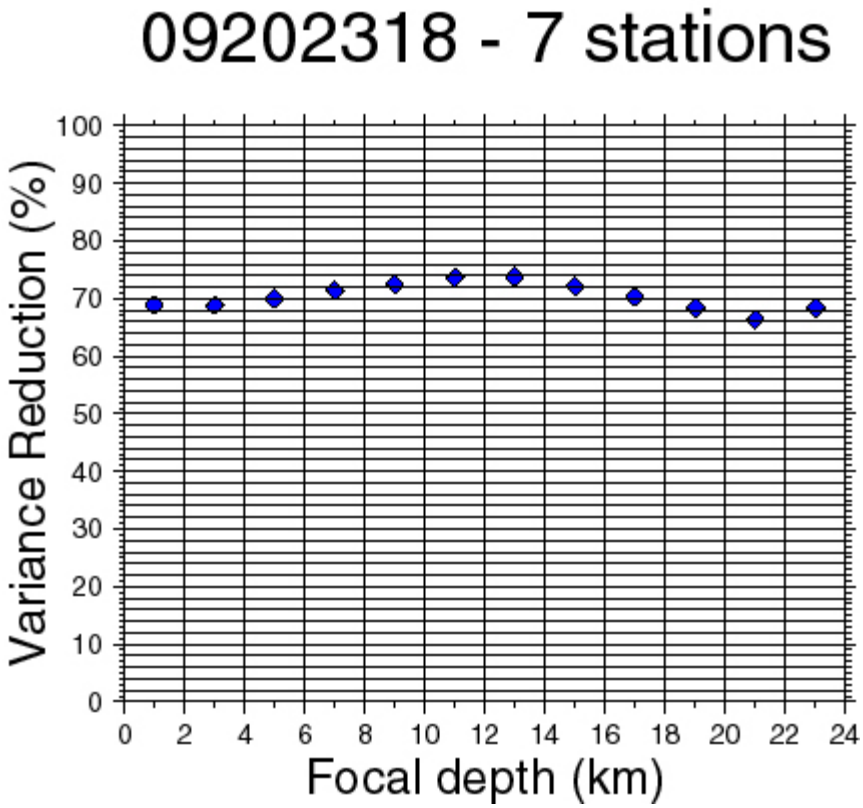

Figure 3.2. The variance reduction is plotted against focal depth for event 23:18 (UTC). The resolution of depth for this event is not good, however a subdued maximum is found at a source depth of 13 km.

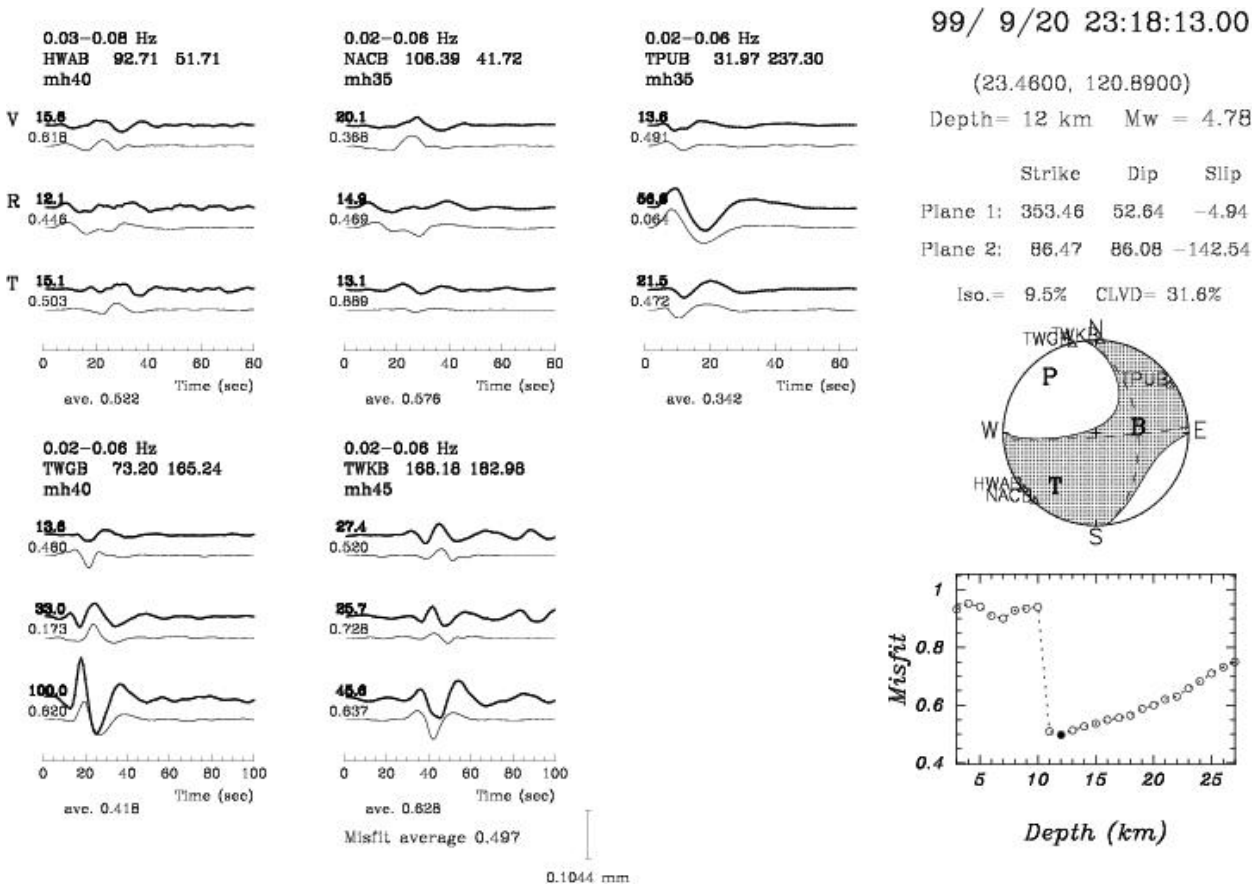

Figure 3.3. Results of Honn Gao using the BATS data for event 23:18 (UTC). The mechanism and focal depth he found is similar to our solution.

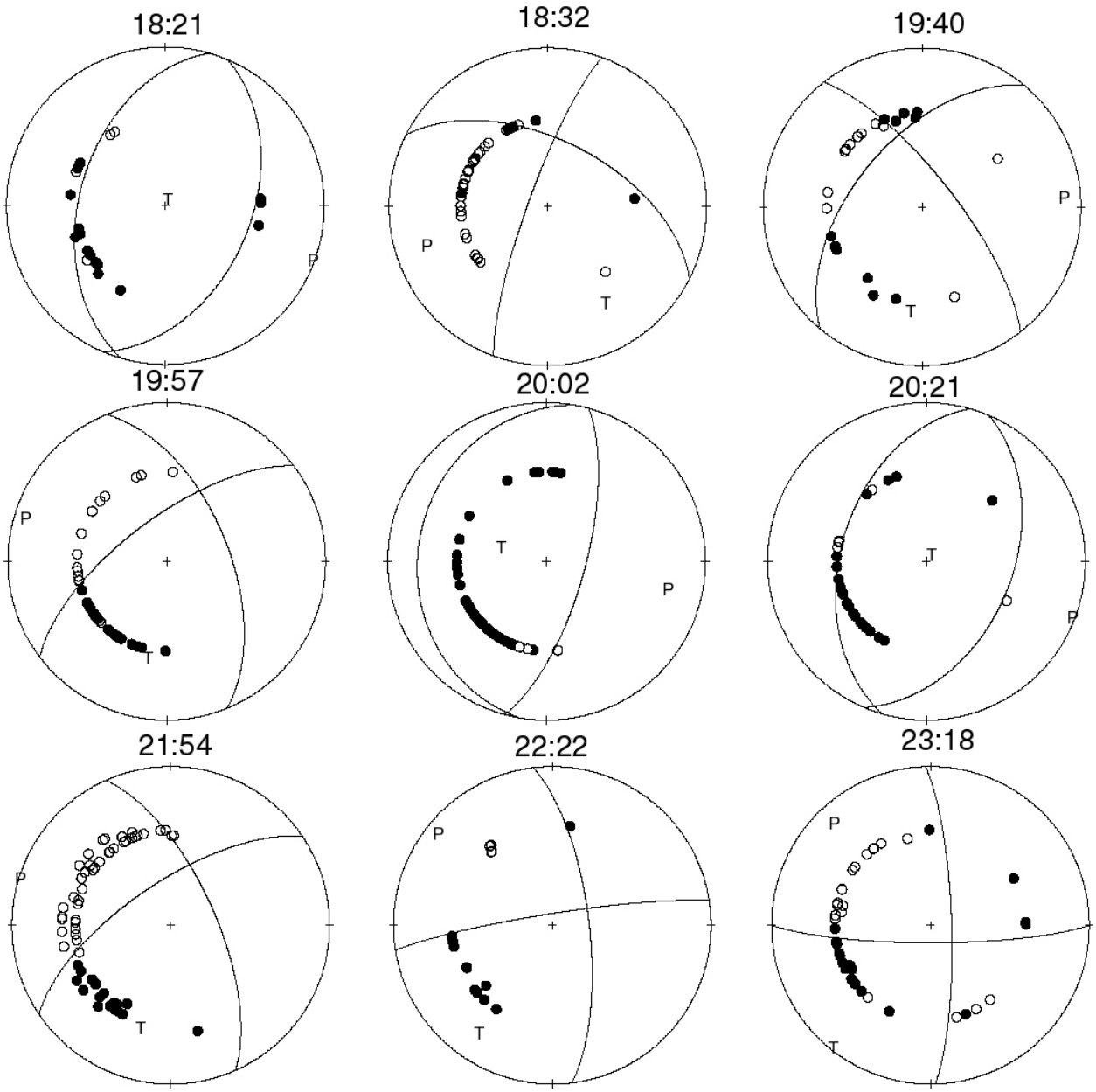

Figure 3.4. First motion solutions for the 9 magnitude 5 aftershocks. Compression first motions are solid, and dilations are open.

Table 3.1. Moment tensor inversion results for M5+ aftershocks

Data	Origin time	depth	Mw	M0	Strike	Rake	Dip	Solution Quality	Faulting Style
1999/09/20	17:57:15.31	21	6.0	1.33E+25	70/177	141/27	68/54	good	oblique-reverse
1999/09/20	18:03:41.16	9	6.3	3.85E+25	204/348	106/57	68/27	good	reverse
1999/09/20	18:21:28.60	-	-	-	-	-	-	Data noisy	-
1999/09/20	18:32:55.07	-	-	-	-	-	-	Data noisy	-
1999/09/20	19:40:32.57	3	5.41	1.58E+24	237/338	141/18	75/53	marginal	oblique-reverse
1999/09/20	19:57:52.63	-	-	-	-	-	-	Data noisy	-
1999/09/20	20:02:15.90	-	-	-	-	-	-	Data noisy	-
1999/09/20	20:21:59.67	-	-	-	-	-	-	Data noisy	-
1999/09/20	21:46:37.49	13	6.3	3.75E+25	243/334	172/2	88/82	good	strike-slip
1999/09/20	21:54:47.08	9	5.1	4.92E+23	236/336	155/24	68/67	good	oblique-reverse
1999/09/20	22:22:46.00	5	4.9	2.59E+23	261/353	161/6	84/71	good	strike-slip
1999/09/20	23:18:13.21	13	4.8	2.09E+23	90/358	-169/-9	81/79	good	strike-slip
1999/09/22	00:14:40.77	21	6.2	2.57E+25	195/292	107/8	88/8	good	reverse
1999/09/25	23:52:49.63	15	6.4	4.19E+25	194/344	106/64	59/34	good	reverse

Table 3.2 First Motion Solutions

Date	***Event ID***	***Strike***	***Dip***	***Rake***	***Style of Faulting***
1999/09/20	18:21:28.60	Not stable			reverse
1999/09/20	18:32:55.07	Not stable			oblique
1999/09/20	19:40:32.57	220	55	160	oblique-reverse
1999/09/20	19:57:52.63	233	68	145	oblique-reverse
1999/09/20	20:02:15.90	190	20	85	reverse
1999/09/20	20:21:59.67	Not stable			reverse
1999/09/20	21:54:47.08	236	68	155	oblique-reverse
1999/09/20	22:22:46.00	261	84	161	strike-slip
1999/09/20	23:18:13.21	90	81	-169	strike-slip

4. Finite Fault Analysis

We used strong motion data to invert the representation theorem (equation 1) for finite source parameters (e.g. Hartzell and Heaton, 1983; Dreger and Kaverina, 2000). The observed seismogram is related to the spatio-temporal integration of slip distributed on a plane where,

$$U_n(x,t) = \int_{-\infty}^{\infty} d\tau \iint_{\Sigma} [u_i(\xi,\tau)] C_{ijpq} \nu_j \partial G_{np,q}(x, t-\tau; \xi, 0) d\Sigma \quad (1)$$

U_n	nth component of observed displacement
C_{ijpq}	elasticity tensor
υ_j	fault orientation unit vector
u_i	fault slip
$G_{np,q}$	Velocity Green's function
x	vector describing the relative location of the source and receiver
ξ, τ	spatial and temporal variables of integration
$d\Sigma(\xi)$	Area differential, Σ is a function of the spatial variable ξ.

The subscript letter n refers to the ground motion component and i, j, p, q are orientation indices. The quantity $C_{ijpq}\upsilon_j u_i(\xi,\tau)$ is equivalent to $m_{ij}(\xi,\tau)$, which describes the spatial and temporal seismic moment tensor. $u(\xi,\tau)$ is the spatio-temporal slip information to be determined by inverting the data.

We use a linear least-squares inversion of observed velocity seismograms to compute the finite-source kinematic models. Several constraining equations are applied to improve the stability of the inversion. These include the requirement that slip is positive (the fault cannot slip backward), and mimimization of the spatial derivative of slip to smooth the results. The strength of the smoothing constraint is controlled by a weight, which is determined iteratively by searching for smoothed models that produce an acceptable level of fit to the waveform data. Although our method allows for multiple time windows to image rupture velocity and rise time heterogeneity, which we found to be very important for the mainshock (Chi et al., 2001), for the aftershocks we assume a single time window and examine the sensitivity of the rupture velocity and average slip rise time parameters on the ability to fit the seismic waveform data. In addition to the rupture velocity and rise time, we examined the sensitivity of the solutions for the fault orientation, and the choice of nodal plane since for the aftershocks surface offsets were not available. The sensitivity of the results to errors in the hypocenter was also examined. In sum, for each of the events, approximately 1000 finite-source inversions were performed. Figure 4.1 shows the parameter space search for the best fault plane orientation and rupture velocity for the aftershock on 1999/09/25 at 23:52:49.63 (Event 5). Figure 4.2 shows the fit to the velocity data, which is good at the stations that have large amplitudes. Figure 4.7 shows the slip distribution that was obtained for the east dipping fault plane. The peak-slip in the model is 170 cm, and slip is distributed over an approximately 20x5 km^2 asperity that extends updip from the hypocenter. The surrounding patches with slip less than 30cm are likely to be artifacts. A detailed discussion of the modeling of this event can be found in (Chi and Dreger, 2002).

The scalar seismic moment was found to be 3.69e+25 dyne cm equivalent to a Mw 6.3. This is significantly less then the reported M_L of 6.8 (Table 1.1), but is consistent with the values obtained in our seismic moment tensor inversions and those of others (e.g. Harvard, Academia Sinica, the U. S. Geologic Survey, and Caltech). The finite-source parameters and the seismic moment from the moment tensor analysis and the Harvard CMT are compared in Table 4.1. The magnitudes of the events will be discussed further in section 5.

The slip models for all of the 6 largest aftershocks are shown in Figures 4.3-4.8, and Table 4.1 lists the parametric information from the finite-source analyses.

The finite-source results were delivered to Brian Chiou of Caltrans as the following email attachments.

HYPOdata.txt - event hypocenter information. The moment and stress drop was computed using only slip that exceeded 10% of the maximum slip value. This is done as a simple way to eliminate contributions from the edges of the model with low slip amplitude and which is poorly constrained.

09201757slip.txt, 09201803slip.txt, 09202146slip.txt, 09220014slip.txt, 09252352slip.txt, 10220218slip.txt - ascii files that contain longitude, latitude, depth (km) and slip (cm) of all of the subfaults in the model. The subfaults are 1x1 km^2 in every case. The values for all subfaults as requested. There are numerous subfaults that have either zero slip or very low levels with respect to the the maximum slip. As a rule of thumb we prefer to interpret only those subfaults that have at least 10% of the maximum slip.

09201757slip.pdf, 09201803slip.pdf, 09202146slip.pdf, 09220014slip.pdf, 09252352slip.pdf, 10220218slip.pdf - These pdf files are images of the slip model for each event. They can be used as a reference when utilizing the ascii files above. In each case the hypocenter is shown as a white square, and the black rectangle (parallel to strike as requested) is the area of the fault that I would be comfortable with in terms of it being interpreted as the fault area to compute the distances to the stations. I would however prefer smaller areas that encompass the main slip patches be used.

These files can be obtained from
http://www.seismo.berkeley.edu/~dreger/peer_chichiaftershocks.zip.

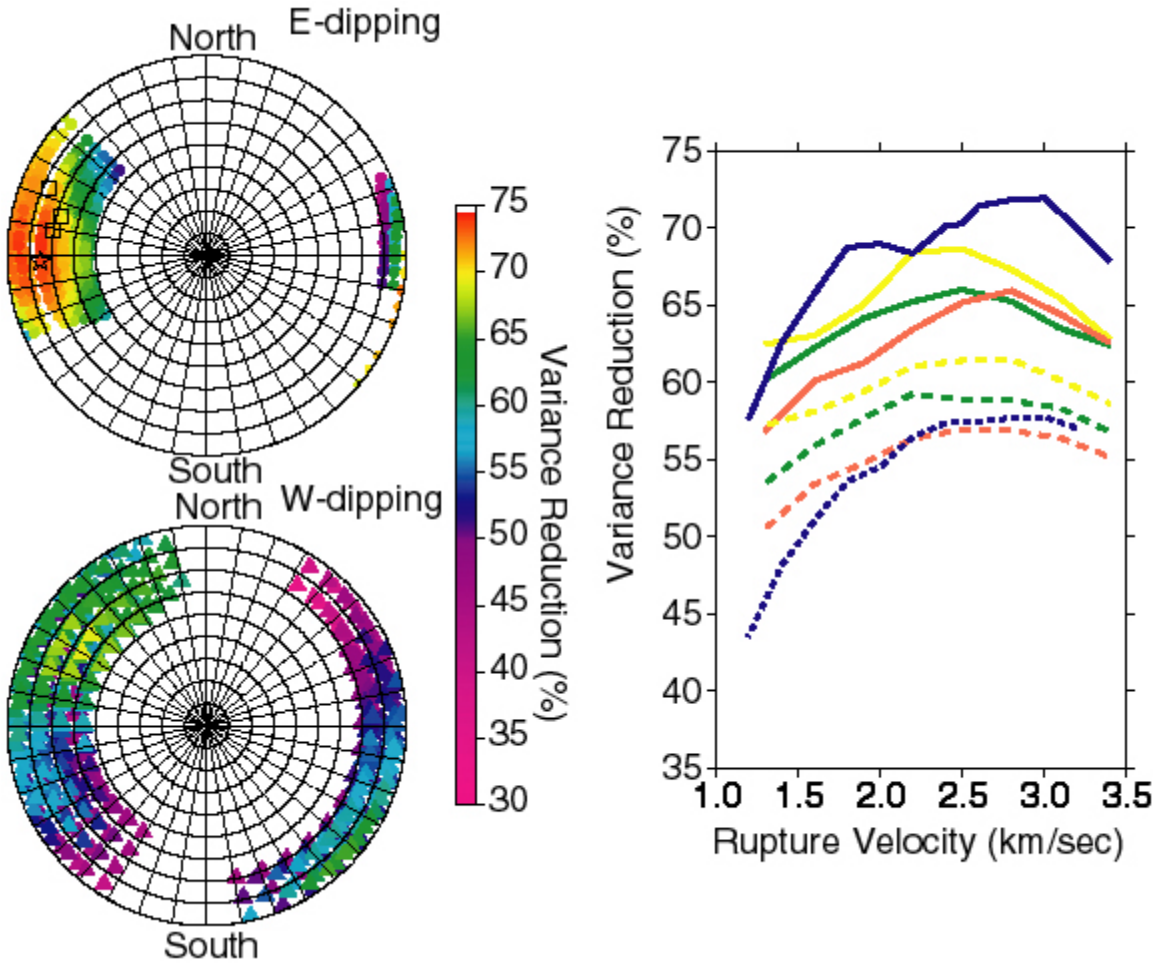

Figure 4.1. On the left the orientation of the P-axes for both the east and west dipping planes for the event on 1999/09/25 (Table 1.1) are plotted with the color corresponding to the level of fit. The east dipping plane was found to fit significantly better. The squares show the orientations of several teleseismic moment tensor solutions, and the star shows the preferred orientation based on the finite-source analysis. For this event we were able to obtain fits of 72% variance reduction. On the right curves comparing the rupture velocity to the variance reduction are shown. The solid curves are for planes with the general preferred orientation and the blue curve is for the best orientation based on the analysis on the left. The focal parameters for this curve are listed on Table 4.1. The dashed curves are for planes with the conjugate orientation.

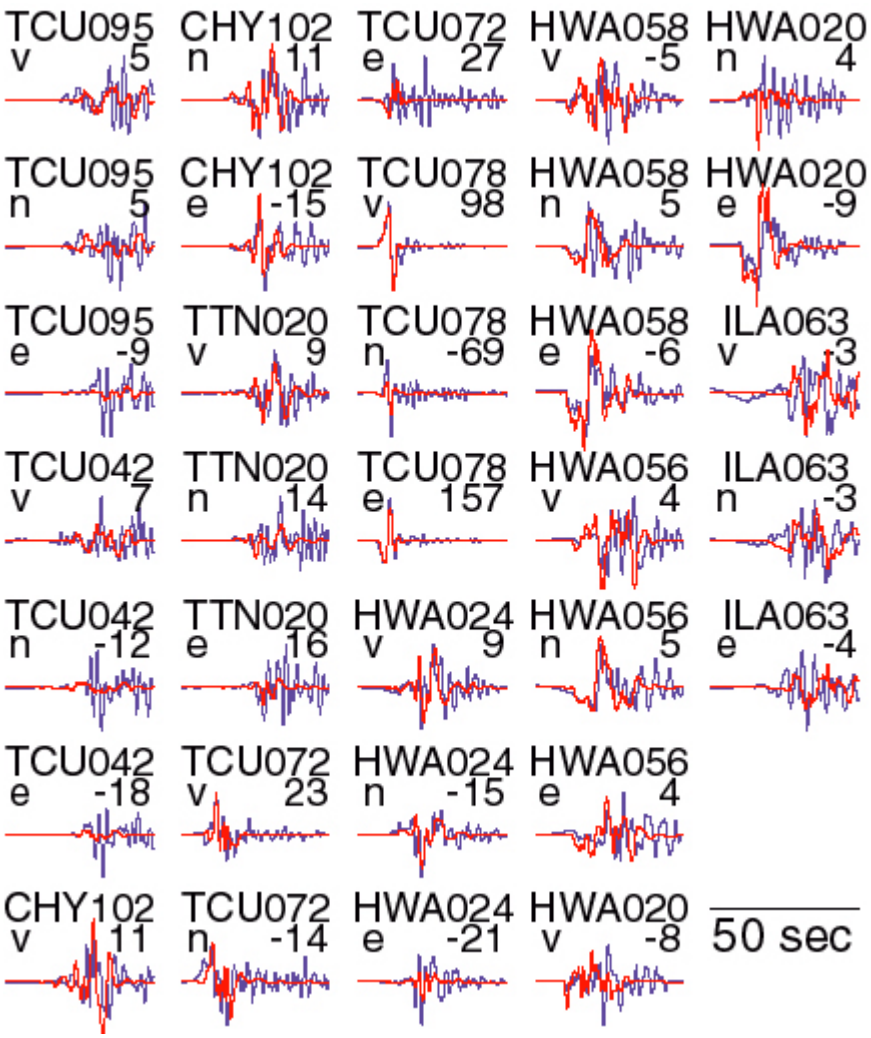

Figure 4.2. Comparision of observed (blue) and predicted (red) velocity seismograms for the event on 1999/09/25 (Table 1.1). The peak velocity in mm/s is plotted for each record beneath the station name.

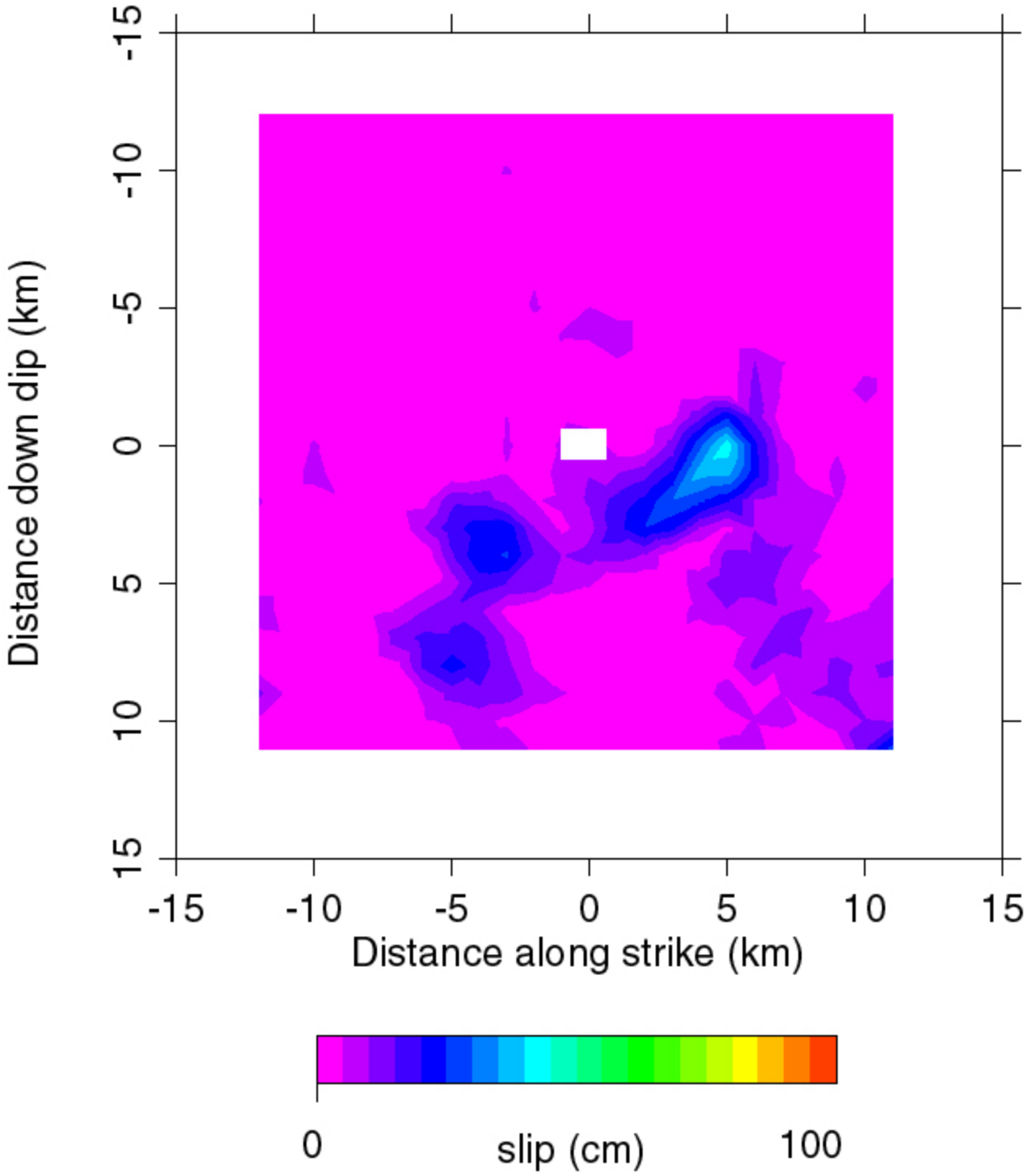

Figure 4.3. Best fitting slip distribution for the aftershock on 1999/09/20 at 17:57 UTC (Event 1). The hypocenter is shown as a white square. See Table 4.1 for parametric information.

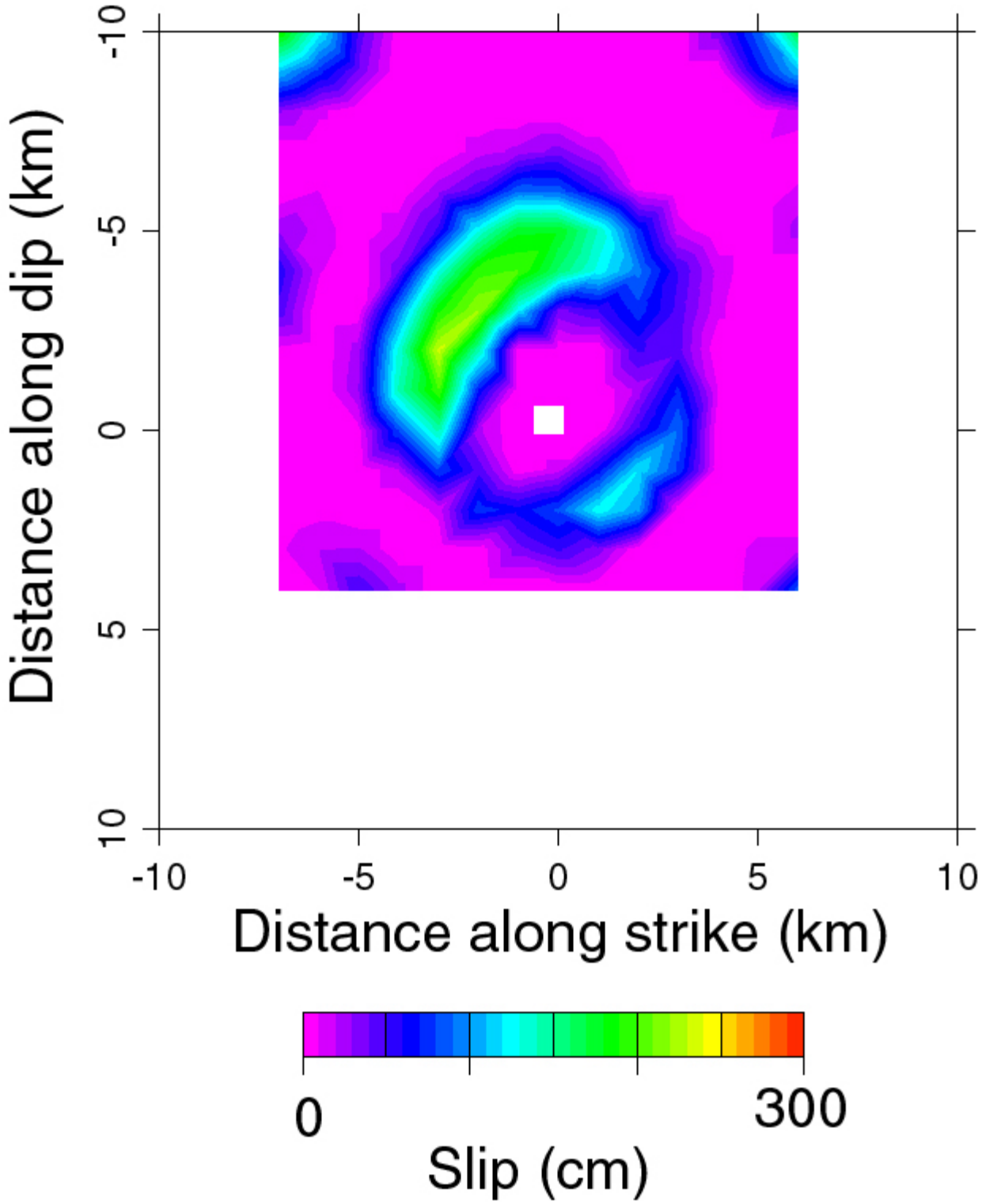

Figure 4.4. Best fitting slip distribution for the aftershock on 1999/09/20 at 18:03 UTC (Event 2). The hypocenter is shown as a white square. See Table 4.1 for parametric information.

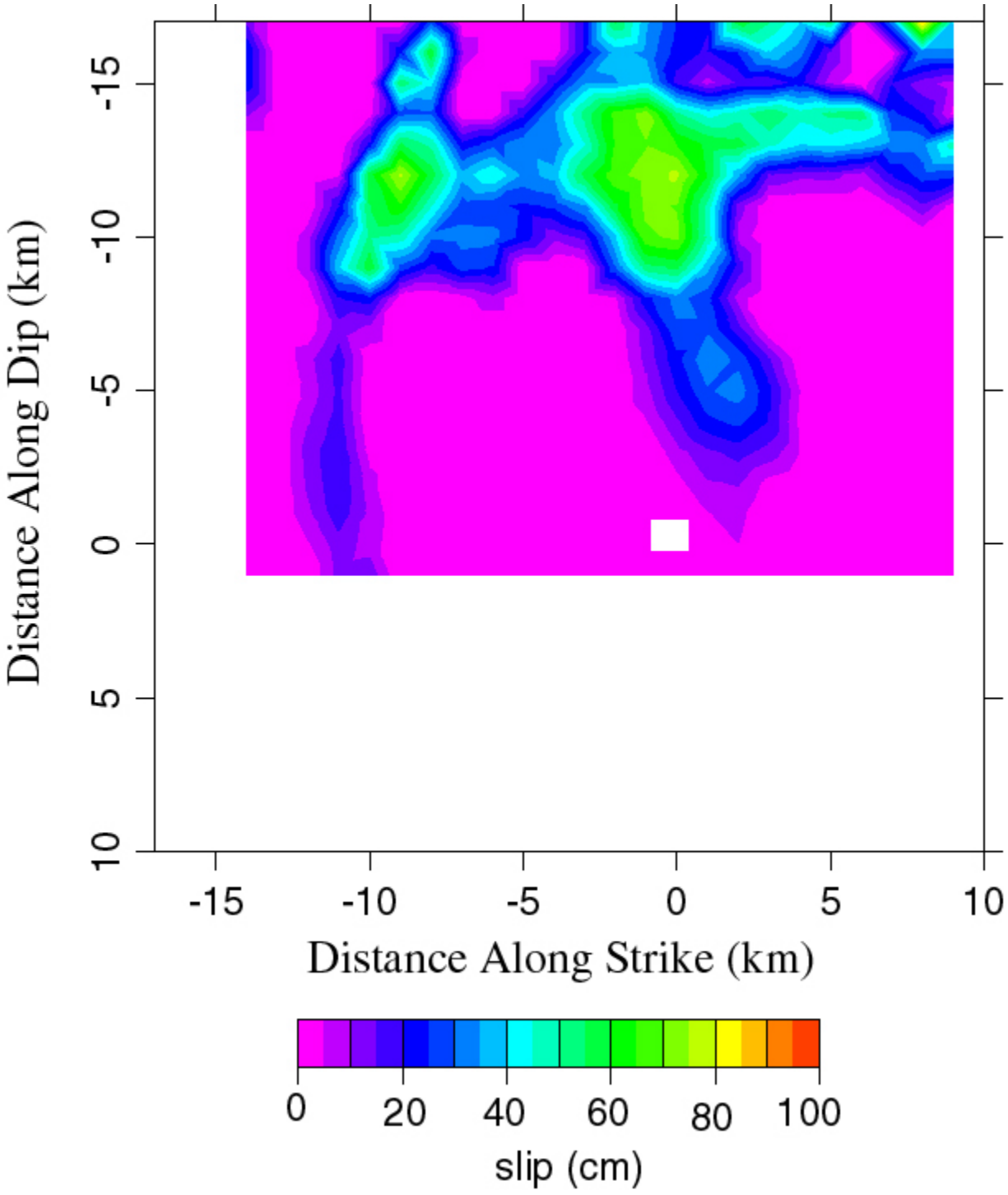

Figure 4.5. Best fitting slip distribution for the aftershock on 1999/09/20 at 21:46 UTC (Event 3). The hypocenter is shown as a white square. See Table 4.1 for parametric information.

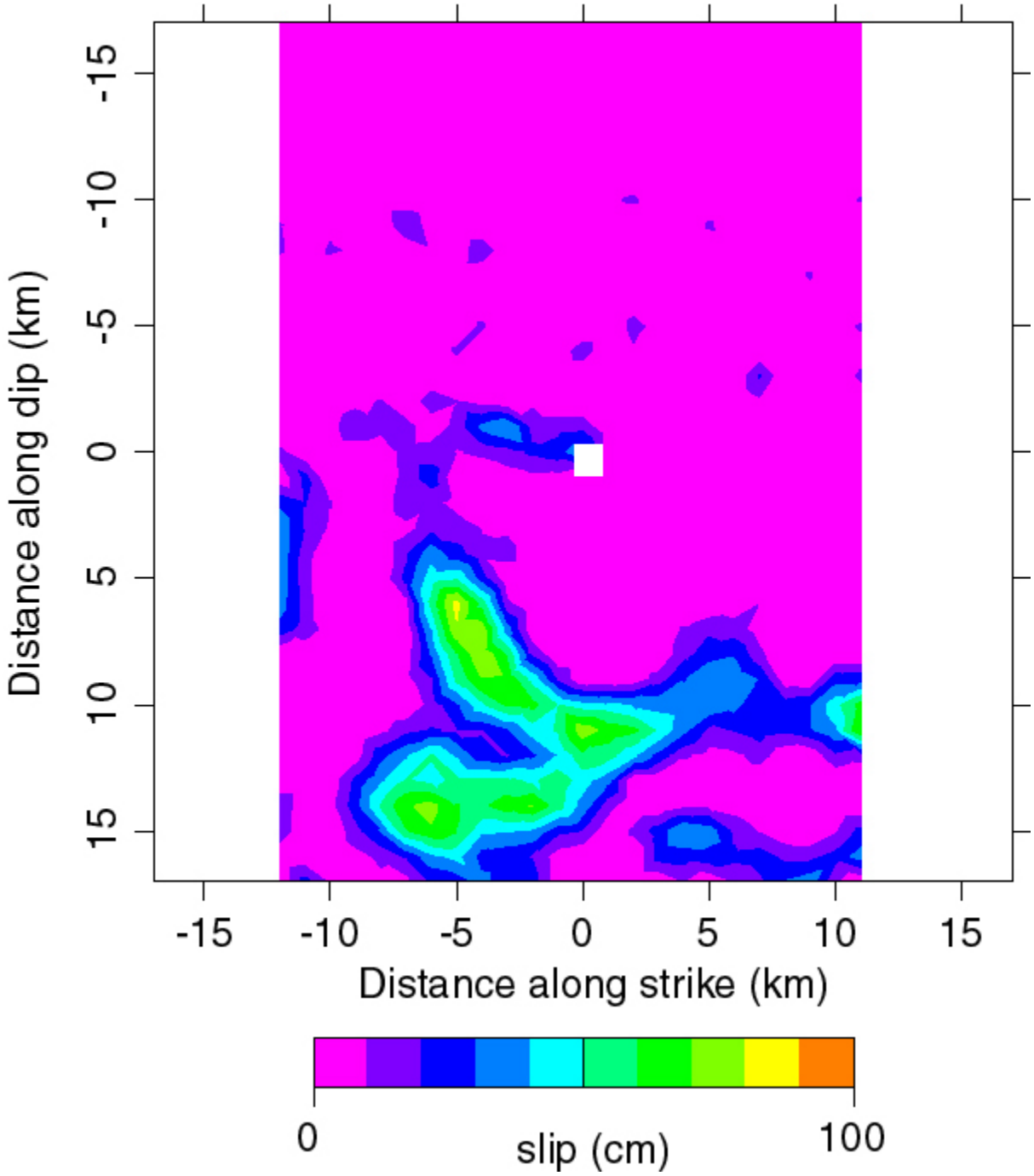

Figure 4.6. Best fitting slip distribution for the aftershock on 1999/09/22 at 00:14 UTC (Event 4). The hypocenter is shown as a white square. See Table 4.1 for parametric information.

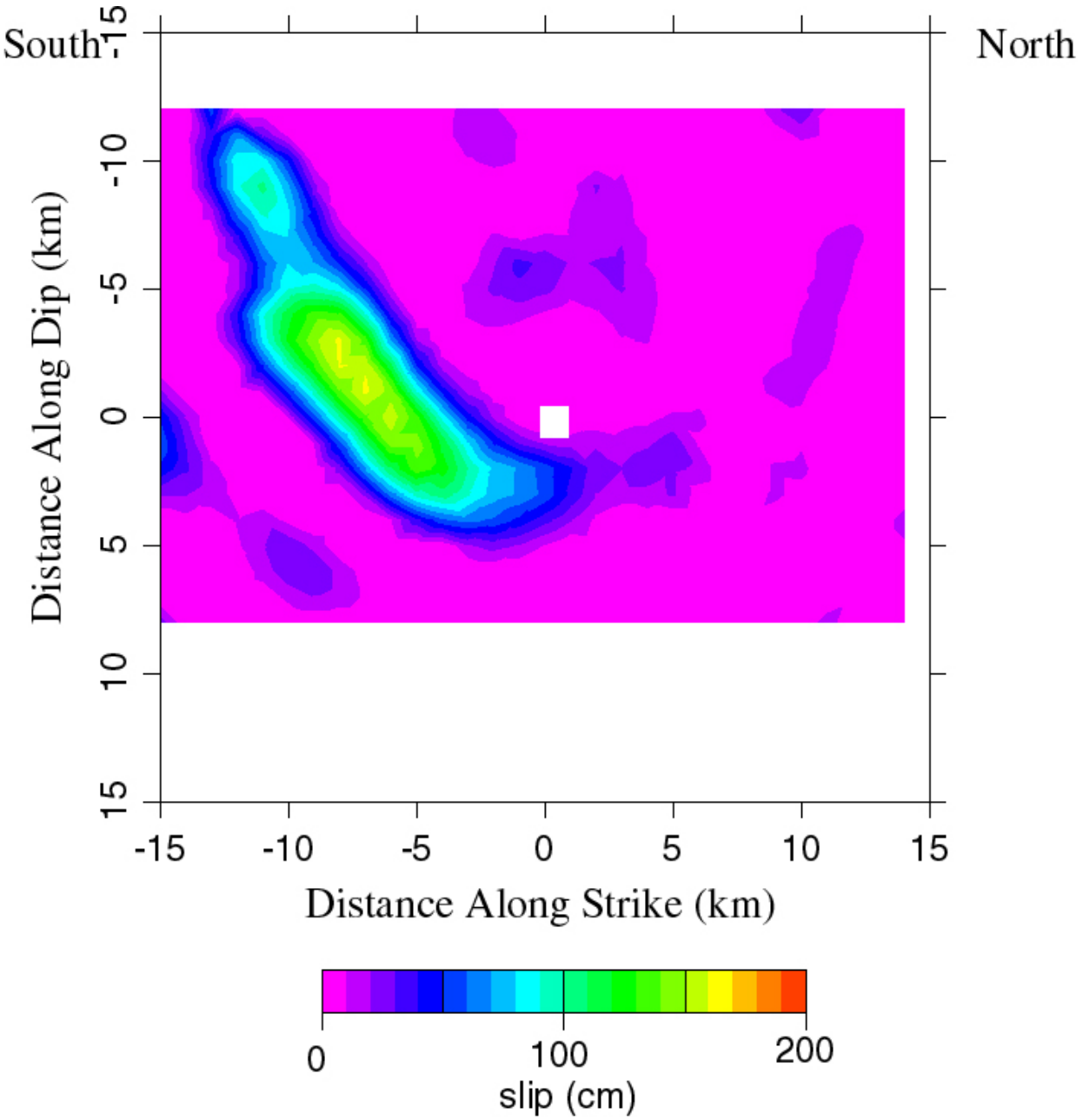

Figure 4.7. Best fitting slip distribution for the aftershock on 1999/09/25 at 23:52 UTC (Event 5). The hypocenter is shown as a white square. See Table 4.1 for parametric information.

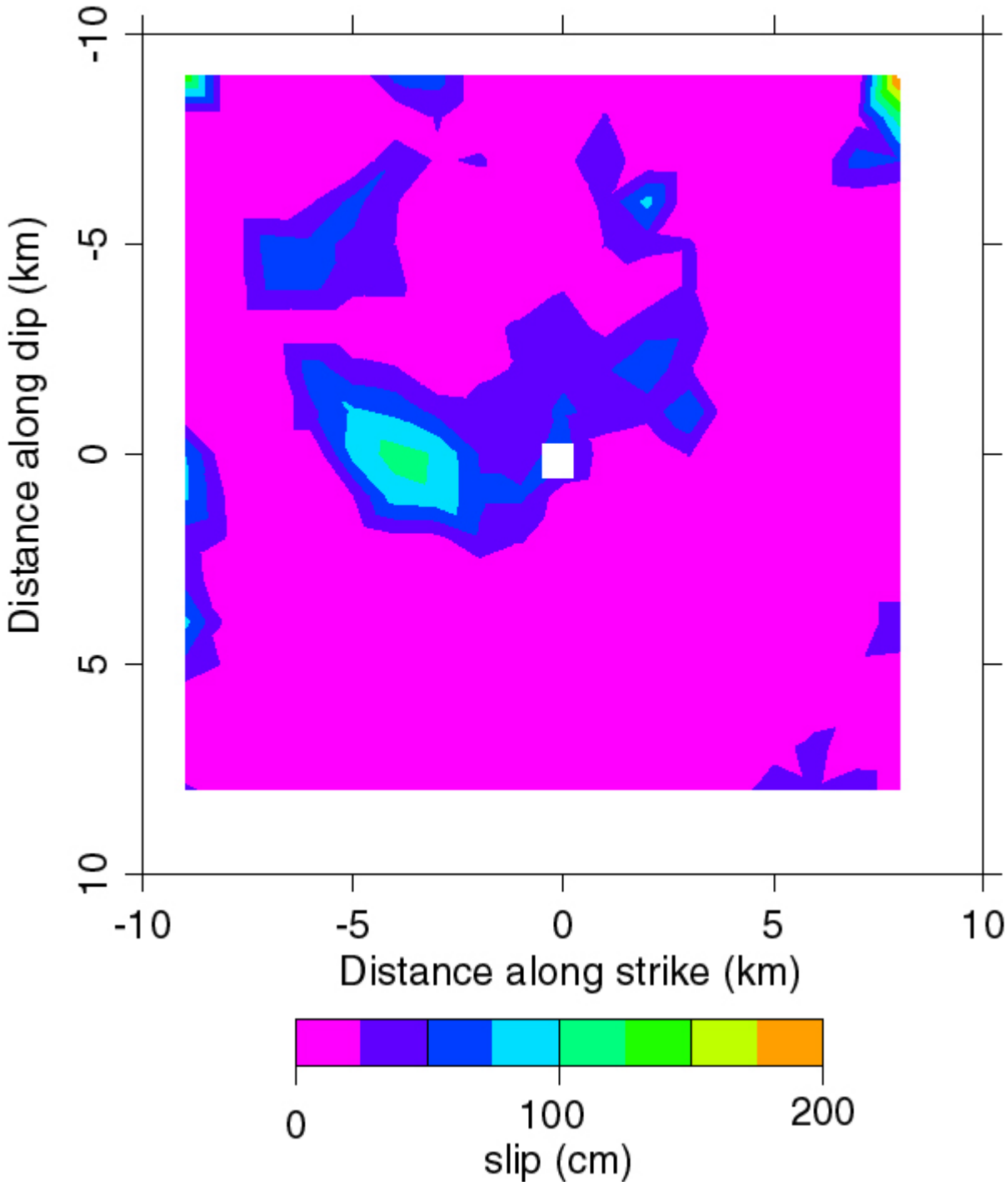

Figure 4.8. Best fitting slip distribution for the aftershock on 1999/10/22 at 02:16 UTC (Event 6). The hypocenter is shown as a white square. See Table 4.1 for parametric information. This event was not on the original list of events to study, but we included it since we had access to the data. The acceleration data was provided to Brian Chiou for use in his analysis of strong ground motion attenuation.

Table 4.1 Finite-Source Parametric Information

Id	Origin Time (mo/dy/yr; hr:min)	Lat, lon., depth	Moment (dyne cm)	Str/rake/dip	Rise time	Rup. Vel.	M_W (FF)	M_W (CW)	Harvard		Original Event Data	
									Mag	Dep.	Mag.	Depth
1	09/20/99; 17:57	23.94, 121.01, 8	7.26E+24	35/100/50	0.2	1.5	5.9	6.0	_	_	6.4	11
2	09/20/99; 18:03	23.81, 120.85, 8	2.53E+25	0/80/10	0.2	1.6	6.2	6.3	_	_	6.6	8
3	09/20/99; 21:46	23.60, 120.82, 18	2.18E+25	330/15/89	0.7	2.4	6.2	6.3	6.4	20	6.6	1
4	09/22/99; 00:14	23.81, 121.08, 10	2.55E+25	165/100/70	0.7	2.6	6.2	6.2	6.4	28	6.8	15
5	09/25/99; 23:52	23.87, 121.01, 16	3.69E+25	5/100/30	0.3	3.2	6.3	6.4	6.5	17	6.4	12
6	10/22/99; 02:16	23.51, 120.40, 18	1.64E+25	200/80/15	0.3	2.2	6.1	_	5.8	15	_	_

5. M_W/M_L Relationship

We have compiled Mw from 4 independent sources in addition to the values estimated in this study. As Figure 5.1 shows there is excellent agreement between the Mw estimates for each event. Generally Mw is less than the reported M_L. A M_W/M_L relationship is provided in Figure 5.1. Interestingly for the mainshock M_L is less than M_W in opposition to what is observed for the aftershocks. This reflects saturation of the M_L magnitude scale for the mainshock, and the arrow shows where the value should plot without saturation. The M_W/M_L relationship may be used to convert the provided M_L to M_W in the magnitude range from 4 to 7.

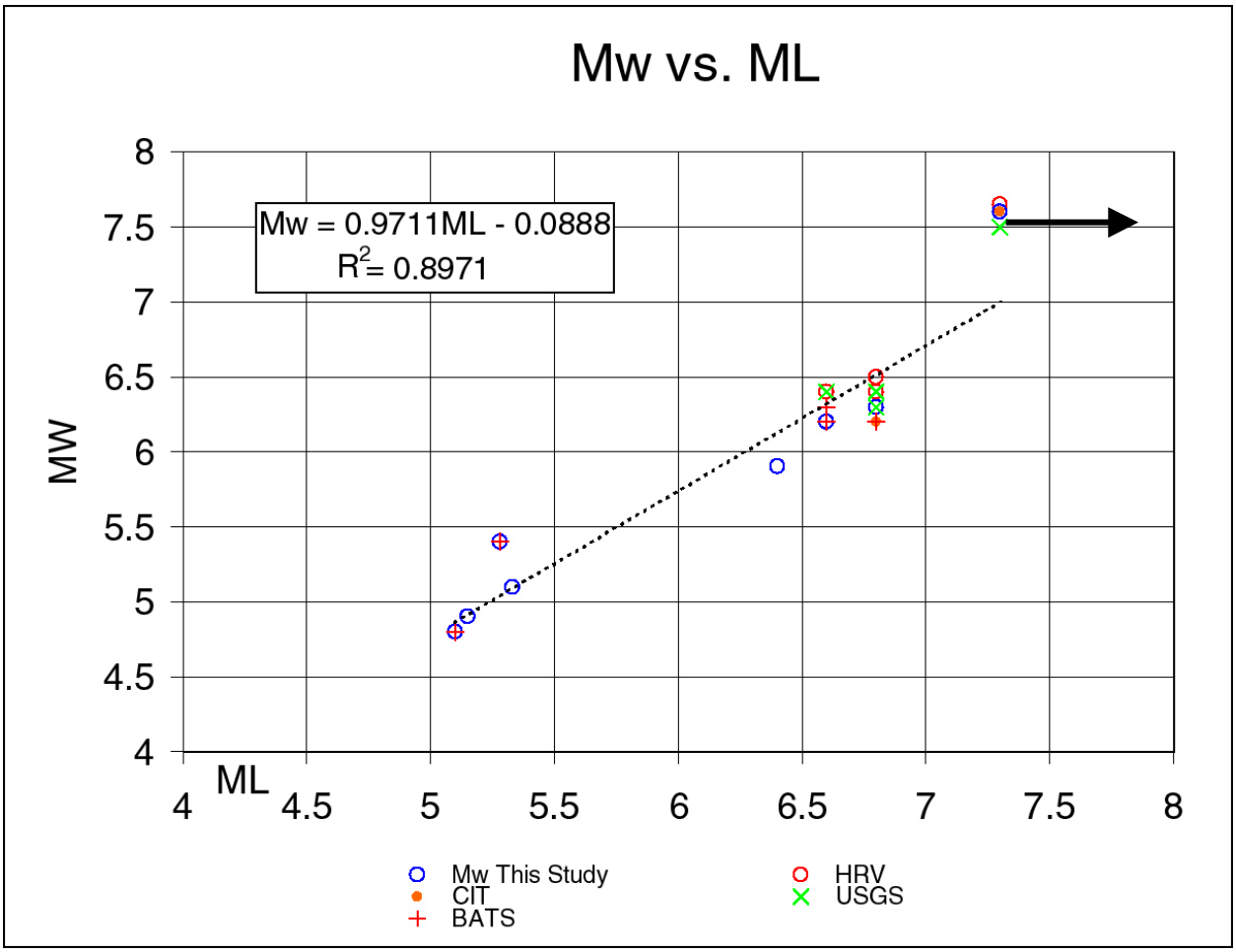

Figure 5.1 Mw obtained from this study, Caltech (CIT), Academia Sinica (BATS), Harvard (HRV) and the USGS are plotted against the M_L provided to this study (e.g. Table 1.1). The best fitting line for the Mw obtained in this study is shown with the M_W/M_L relationship.

6. Conclusions

We have examined the strong motion acceleration waveform data for 30 aftershocks of the September 20, 1999 M_W7.6 Chi-Chi, Taiwan earthquake sequence. For the $5.0 \leq M_W < 6.0$ aftershocks we measured P and S arrival times and the first motion polarity. Using a grid search method the events were relocated. We found that the locations that were initially provided to the project (Table 1.1) are adequate for use in developing attenuation relationships. The average change in location was only 3.8 km with a total range from 1.2 to 7.5 km. The relocations are listed in Table 2.1. If they are used it is recommended that they be combined with the source depths determined in the moment tensor analysis (Table 3.1).

Four of the M5 events and the 6 M6 events were studied using a seismic moment tensor inversion. Scalar seismic moment and Mw were determined for these events (Table 3.1). Style of faulting information (strike-slip, oblique-reverse, and reverse) is reported in Table 3.1 from the moment tensor analysis and in Table 3.2 from the first-motion polarity analysis.

The six largest aftershocks were analyzed using a finite-source inverse methodology. For each event approximately 1000 inversions were performed to determine the orientation of the rupture plane, as well as the sensitivity of the rupture velocity, dislocation rise time, and hypocenter location parameters. These parameters are listed in Table 4.1. The slip models have been delivered to Brian Chiou and can be obtained from;

http://www.seismo.berkeley.edu/~dreger/peer_chichiaftershocks.zip

Two peer-reviewed publications on the finite-source analysis have been completed as a result of this study (Chi and Dreger, 2002; Chi and Dreger, 2004). The Chi and Dreger (2002) publication may be obtained from;

http://www.seismo.berkeley.edu/~dreger/ChiandDreger2002GRL.pdf

The Chi and Dreger (2004) is presently undergoing final revisions. It will be made available at:

http://www.seismo.berkeley.edu/~dreger/ChiandDreger2004GRL.pdf

Unfortunately due to the high levels of low frequency noise in the passband used to determine seismic moment tensors M_W was only determined for 10 events. The M_W from the moment tensor analysis and the finite-source analyses agree closely, and in addition, the obtained M_W agrees extremely well with values obtained by Caltech, Harvard, Academia Sinica, and the U.S. Geological Survey. These other agencies did not compute solutions for any of the events that we were not able to obtain source parameters for.With this limited data set we derived a relationship (Figure 5.1) between M_W and M_L. This relationship may be used to convert the provided M_L to M_W in the magnitude range from 4 to 7.

Finally, it is noted that there are a number of other M6 aftershocks not contained on the event list provided to this project but now have seismic waveform data available from the Central Weather

Bureau. Future studies of these events can provide additional constraints on the fault structure activated by the mainshock and also on the nature of strong ground motion attenuation.

7. References

Chi, W.C., D. Dreger, and A. Kaverina (2001) Finite-source modeling of the 1999 Taiwan (Chi-Chi) earthquake derived from a dense strong-motion network, Dedicated issue on the Chi-Chi, Taiwan earthquake of 20 September 1999, Bull. Seism. Soc. Am., vol.91, no.5, pp.1144-1157.

Chi, Wu-Cheng and Douglas Dreger (2002), Finite Fault Inversion of the September 25, 1999 (Mw=6.4) Taiwan Earthquake: Implications for GPS displacements of Chi-Chi, Taiwan Earthquake Sequence, Geophysical Research Letters, Vol. 29, no. 14, doi: 10,1029/2002GL015237.

Chi, Wu-Cheng and Douglas Dreger (2004), Seismic Hazard Mitigation and Crustal Deformation: Results from Finite Source Processes of Six Mw > 5.8 Chi-Chi, Taiwan Aftershocks, in review Journ. Geophys. Res.

Dreger, D. S. and A. Kaverina (2000). Seismic remote sensing for the earthquake source process and near-source strong shaking: a case study of the October 16, 1999 Hector Mine earthquake, *Geophys. Res. Lett.,* 27, 1941-1944.

Dreger, D., R. Uhrhammer, M. Pasyanos, J. Franck, and B. Romanowicz (1998). Regional and Far-Regional Earthquake Locations and Source Parameters using Sparse Broadband Networks: A Test on the Ridgecrest Sequence, *Bull. Seism. Soc. Am*., 88, 1353-1362.

Fukuyama, E., and D. Dreger (2000). Performance test of an automated moment tensor determination system for the future "Tokai" earthquake, Earth Planets Space, 52, 383-392.

Kaverina, A., D. Dreger, and E. Price (2002). The combined inversion of seismic and geodetic data for the source process of the 16 October, 1999, Mw7.1 Hector Mine, California, earthquake, *Bull. Seism. Soc. Am*. *Special Issue*.

Hartzell, S. H., and T. H. Heaton (1983). Inversion of strong ground motion and teleseismic waveform data for the fault rupture history of the 1979 Imperial Valley, California, earthquake, *Bull. Seism. Soc. Am.,* 73, 1553-1583.

Pasyanos, M. E., D. S. Dreger, and B. Romanowicz (1996). Toward real-time estimation of regional moment tensors, *Bull. Seism. Soc. Am*., 86, 1255-1269.

Romanowicz, B. D. Dreger, M . Pasyanos, and R. Urhammer (1993). Monitoring of Strain Release in Central and Northern California Using Broadband Data, Geophys. Res. Let., 20, 1643-1646.

Uhrhammer, R. A., D. Dreger and B. Romanowicz (2001). Best practice in earthquake location using broadband three-component seismic waveform data, Pure. Appl. Geophys., 158, 259-276.

Wessel, P., and W. H. F. Smith (1991). Free software helps map and display data, EOS, 445-446.